Article

Synthesis and Electrochemical Performance of Mesoporous NiMn$_2$O$_4$ Nanoparticles as an Anode for Lithium-Ion Battery

Swapnil J. Rajoba [1,*]**, Rajendra D. Kale** [1]**, Sachin B. Kulkarni** [1]**, Vinayak G. Parale** [2]**, Rohan Patil** [3]**, Håkan Olin** [3]**, Hyung-Ho Park** [2]**, Rushikesh P. Dhavale** [2] **and Manisha Phadatare** [3,*]

[1] Post Graduate Research Centre, Department of Physics, Tuljaram Chaturchand, College, Baramati 413 102, India; rajendra_kale@yahoo.com (R.D.K.); sachinkulkarni21@gmail.com (S.B.K.)

[2] Department of Materials Science and Engineering, Yonsei University, 50 Yonsei-ro, Seodaemun-gu, Seoul 03722, Korea; vinayakparale3@gmail.com (V.G.P.); hhpark@yonsei.ac.kr (H.-H.P.); rushi@yonsei.ac.kr (R.P.D.)

[3] Department of Natural Sciences, Mid Sweden University, 851 10 Sundsvall, Sweden; rohan.patil@miun.se (R.P.); hakan.olin@miun.se (H.O.)

[*] Correspondence: swapnilrajoba@gmail.com (S.J.R.); manisha.phadatare@miun.se (M.P.)

Abstract: NiMn$_2$O$_4$ (NMO) is a good alternative anode material for lithium-ion battery (LIB) application, due to its superior electrochemical activity. Current research shows that synthesis of NMO via citric acid-based combustion method envisaged application in the LIB, due to its good reversibility and rate performance. Phase purity and crystallinity of the material is controlled by calcination at different temperatures, and its structural properties are investigated by X-ray diffraction (XRD). Composition and oxidation state of NMO are further investigated by X-ray photoelectron spectroscopy (XPS). For LIB application, lithiation delithiation potential and phase transformation of NMO are studied by cyclic voltammetry curve. As an anode material, initially, the average discharge capacity delivered by NMO is 983 mA·h/g at 0.1 A/g. In addition, the NMO electrode delivers an average discharge capacity of 223 mA·h/g after cell cycled at various current densities up to 10 A/g. These results show the potential applications of NMO electrodes for LIBs.

Keywords: energy storage and conversion; NiMn$_2$O$_4$; XPS; lithium-ion battery; electrochemical performance

1. Introduction

Li-ion battery (LIB) technology is widely used for energy storage application due to its long cycle life, high cell voltage, low self-discharge, high energy and power density, and relatively simple reaction mechanism [1]. Therefore, these batteries are commercially available in several fields, such as portable electronic devices and electric vehicles [2]. The rapid development in mobile electronics and electric cars demands that the next generation of LIB's to be developed. Generally, the electrochemical performance of LIB is governed by specific capacity and working potentials of active material [3]. Most of the commercial LIB's used graphitic carbon as an anode material though its cycling is extremely unstable and rapid loss in capacity is observed at higher current [4]. In recent years, Li$_4$Ti$_5$O$_{12}$ is reported to replace graphitic carbon. It shows excellent lithium insertion/de-insertion properties with a minimum volume change. Still, it has a low specific capacity (175 mA·h/g) and moderate rate performance due to its poor electronic conductivity [5].

Carbon-based materials, alloy materials, silicon, and transition metal oxides are used as an anode to achieve maximum cell capacity [6]. Nowadays, the research of anode material is focused on transition metal oxides, phosphides, sulfides, nitrides, etc. due to its cost effectiveness, availability, and environment friendliness [7]. However, low electronic conductivity (limits electron transfer), significant volume expansion during insertion/deinsertion of Li-ion (damage structure of active materials), and voltage hysteresis

(leads to low energy efficiency) are the main challenges in the commercialization of these materials [8]. Therefore, to enhance the electrochemical performance of anode material, researchers have focused on resolving these issues.

Among transition metals, AB_2O_4 compounds (where A is divalent cation and B is trivalent cation) are more attractive compared to other metal oxides because of coexistence of two distinct cations in the single crystal [9]. Furthermore, researchers have synthesized these compounds with various morphologies such as nanotubes, nanowires, nanoflakes, etc. to boost its storage performance [10]. However, the comprehensive performance of all LIB's with these compounds is being still improved to meet the requirements of modern society. Thus, there is a demand to design and synthesize nanomaterials as an anode for LIBs.

Given all these issues, $NiMn_2O_4$ (NMO) is one of the promising anode materials for LIBs owing to its higher conductivity and superior electrochemical activity compared to other metal oxides [9]. It offers more redox-active sites due to the lattice position of both Mn and Ni [9,11]. Besides, various oxidation state of manganese provides more accessible sites for redox reaction [10]. It enhances cyclic stability and rate performance [9]. Furthermore, it has more advantages such as abundant availability, low cost, non-toxic nature, and environmental friendliness [12]. Because of these considerations, spinel NMO is potential anode material for the next generation of LIBs.

Considering the significance of NMO and its properties, the solution combustion technique has proposed in the current research work. This method is simple, use relatively simple equipment, and allow control of crystallinity, and dopants can be introduced in the final product [13]. In addition, in this technique, carbon-based fuel was used, which provides in situ carbon coating and limit grain growth and agglomeration [14]. Moreover, in the current research work, the electrodes were fabricated using sodium alginate as a binder due to its extraordinary properties such as rich carboxylic group contents, high Young's modulus and electrochemical stability. It leads to enhance specific capacity, cyclic stability, and coulombic efficiency [15].

2. Experimental Procedure

2.1. Materials and Methods

NMO nanoparticles were synthesized by solution combustion synthesis (SCS) technique. Nickel nitrate ($Ni(NO_3)_2.6H_2O$, Alfa Aesar 98%) and manganese nitrate ($Mn(NO_3)_2.4H_2O$, Sigma Aldrich (St. Louis, MO, USA) >97%) were used as metal precursors. Citric acid ($C_6H_8O_7$, Analytical Reagent AR) was used as a fuel. The metal nitrates precursors were dissolved in the minimum amount of distilled water and kept on a hot plate for constant stirring and heating. Then, citric acid was dissolved in a minimum amount of distilled water and added into the solution of metal nitrate precursor. It makes homogeneous mixture by mixing metal nitrates at the molecular level. The stoichiometric oxidant to fuel ratio was 1:1.12. During constant heating and stirring, excess water was removed, and the gel was formed. This gel was kept in a pre-heated furnace; it was decomposed and black colored ash was formed. After grinding and homogenization of powder in an agate mortar, it was calcined in a muffle furnace at different temperatures for 5 h.

2.2. Material Characterization

The structural and crystalline properties of calcined NMO powder were carried out using X-ray diffractometer (PHILIPS PW-3710) with Cu K_α as the radiation source. The Raman spectrum (Lab RAMA ramis, Horiba Jobin Yvon) was recorded at an excitation wavelength of around 532 nm. Chemical bonding of the powder was studied by Fourier-transform infrared spectroscopy (FTIR PerkinElmer1760X spectrophotometer) at a wavelength ranging from 400 to 3500 cm^{-1}. The oxidation states of the elements present in the system were determined using X-ray photoelectron spectroscopy (XPS) using a K-alpha (Thermo VG, Grinstead, UK) non-monochromatic Al K_α radiation (1486.6 eV). Morphological properties and energy-dispersive X-ray analysis (EDAX) were analyzed

using a field-emission scanning electron microscope (FE-SEM, Hitachi S-4200). The specific surface area was measured by Brunauer–Emmett–Teller (BET) analysis using the amount of N_2 gas adsorbed with the relative pressure (in the range of 0.01 < P/P0 < 1). The total pore volume, average pore diameter, and distribution of pore size were analyzed by the Barrett–Joyner–Halenda (BJH) method using aBET surface analyzer (Quantachrome, Autosorb-iQ, Boynton Beach, FL, USA).

2.3. Electrode Fabrication

To prepare anode, NMO was mixed with carbon black and sodium alginate (as a binder) with a weight ratio of 75:15:10 using a magnetic stirrer. The resultant slurry was cast on copper foil (1 mg/cm^2) to prepare the electrode, out of which active mass of the working material is 0.75 g/cm^2 (excluding 15% carbon black and 10% sodium alginate). The resultant film was dried in an oven at 100 °C overnight and punched into round discs with a diameter of 13 mm. The half-cells of these electrodes were assembled in the argon-filled glove box (H_2O < 0.1 ppm and O_2 < 0.1 ppm). Lithium metal foil was used as a reference and counter electrode. Celgard 2325 membrane was used as a separator. 1 Notably, M LiPF$_6$ in ethylene carbonate (EC) and diethyl carbonate (DEC) in a weight ratio of 1:1 was used as an electrolyte. Apparently, 80 μLis the amount of electrolyte used in the half cell.

2.4. Electrochemical Measurement

The cyclic voltammetry tests were performed between 0.01 and 3.0 V at a scan rates of0.01, 0.05, and 0.1 mV/s using a VersaSTAT 4 Potentiostat. The galvanostatic charge–discharge tests of the cells were performed using a LabVIEW-based PXI system in a voltage range between 0.01 and 3.0 V at various current densities. Henceforth, the voltages mentioned were recorded with respect to Li/Li$^+$.

3. Result and Discussion

3.1. Material Analysis

XRD patterns of as-prepared NMO and calcined at 600, 700, and 800 °C are shown in Figure 1. The observed XRD pattern was compared with the standard JCPDS card (71-0852). The reflections (111), (220), (311), (400), (511), and (440) corresponding to NMO were present in all the XRD patterns. Thus, it revealed the formation of cubic crystal structure. However, some additional diffraction peaks were observed in the XRD pattern of as-prepared and powder calcined at 600 and 700 °C, due to the formation of secondary phases. These phases were removed by further calcination at a higher temperature (800 °C) and phase pure NMO was obtained. The average crystalline size (D) of phase pure NMO was calculated using Scherer's formula and was 55 nm.

FTIR spectrum was recorded in the range of 400–3500 cm^{-1} (Supporting Documents Figure S1). The two characteristic bands observed at 503 and 575 cm^{-1} were assigned to the vibrational mode of the octahedral group vibration of Ni^{2+}-O^{2-} and the tetrahedral group of Mn^{3+}-O^-, respectively [10,16]. The band observed at 417 cm^{-1} was assigned to vibration mode of Ni-O-Mn [10]. The appearance of these bands in the FTIR spectrum confirmed single phase formation of spinel structure [16]. In addition, two small intense bands were observed at 843 and 1015 cm^{-1}, which were assigned to the NMO [17].
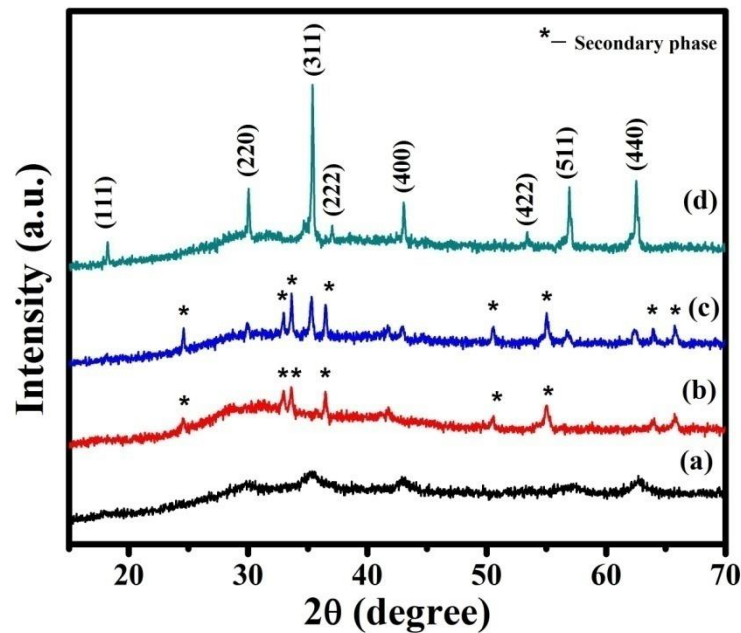
Figure 1. XRD patterns of the samples: (**a**) as-prepared $NiMn_2O_4$(NMO) powder, (**b**) calcined at 600 °C (**c**) calcined at 700 °C, and (**d**) calcined at 800 °C.

The composition and oxidation state of NMO were further investigated by XPS spectrum. Figure 2a–d showed core scan spectra of C 1s, O 1s, Mn 2p, and Ni 2p. The core scan spectra of C 1s (Figure 2a) can be fitted into three peaks, and the peaks observed at 284.3, 285.5, and 287.6 eV were assigned to C=C sp^2 hybridized carbon atom, C-C sp^3 hybridized carbon atom, and C-O and C-OH, respectively. [18]. Owing to the electronic conductivity of sp^2 carbon atom, it can enhance the electrochemical properties of NMO. The core scan spectra of O 1s, showed in Figure 2b, indicated a sharp peak at 529.2 eV because of metal-oxygen bond, whereas the peak observed at 530.6 eV was assigned to defects, contaminants, and chemisorbed oxygen [10]. The core scan spectra of Mn 2p, shown in Figure 2c, it revealed that Mn atoms were present in the electronic configuration Mn $2p_{3/2}$ and $2p_{1/2}$ with a binding energy of 641.06 and 652.74 eV, respectively. The value of spin orbit splitting was about 11.68, and this confirmed the presence of Mn^{3+} state [19]. In addition, the binding energy peak observed at 644.15 and 656.68 eV was assigned to Mn^{2+} and Mn^{4+}, respectively [20]. The core scan spectrum of Ni 2p was shown in Figure 2d. The binding energy peak centered at 854.25 and 871.85 eV was assigned to Ni $2p_{3/2}$ and Ni $2p_{1/2}$, respectively. The satellite peaks observed at binding energies 860.01 and 878.34 eV was assigned to Ni $2p_{3/2}$ and Ni $2p_{1/2}$, respectively [17].

The hexagonal morphology of NMO nanoparticles was observed in field emission scanning electron microscope (FESEM) image (Figure 3). Due to higher calcination temperature, light agglomerated structure was observed with grain size in a range of 200–500 nm. In addition, the presence of elements such as Ni, Mn, and O were justified using EDAX. Residual carbon was observed from the elemental analysis, which helps to avoid agglomeration in calcined material. This residual carbon was considered as a superior conductive substance to enhance the electronic conductivity of material [9]. The average atomic and weight percentage was listed in the inset of Figure 3b.
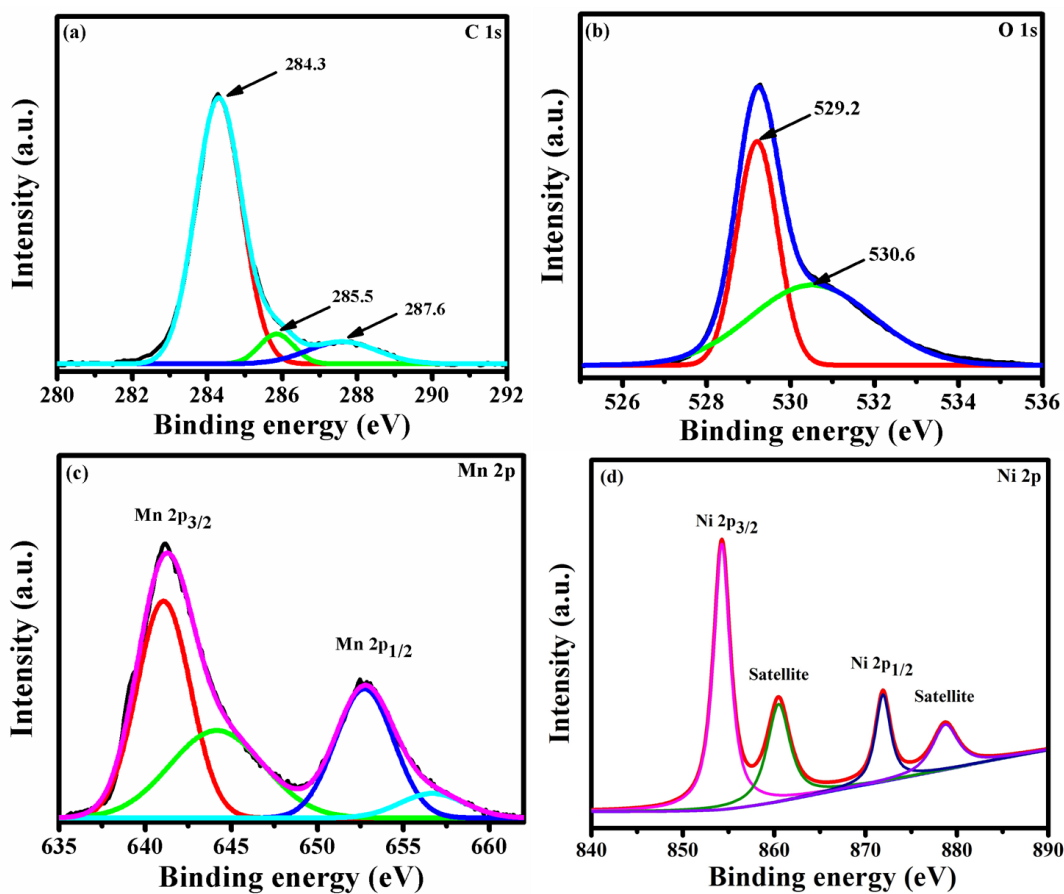
Figure 2. XPS of NMO contains core scan of (**a**) C 1s, (**b**) O 1s, (**c**) Mn 2p, and (**d**) Ni 2p.

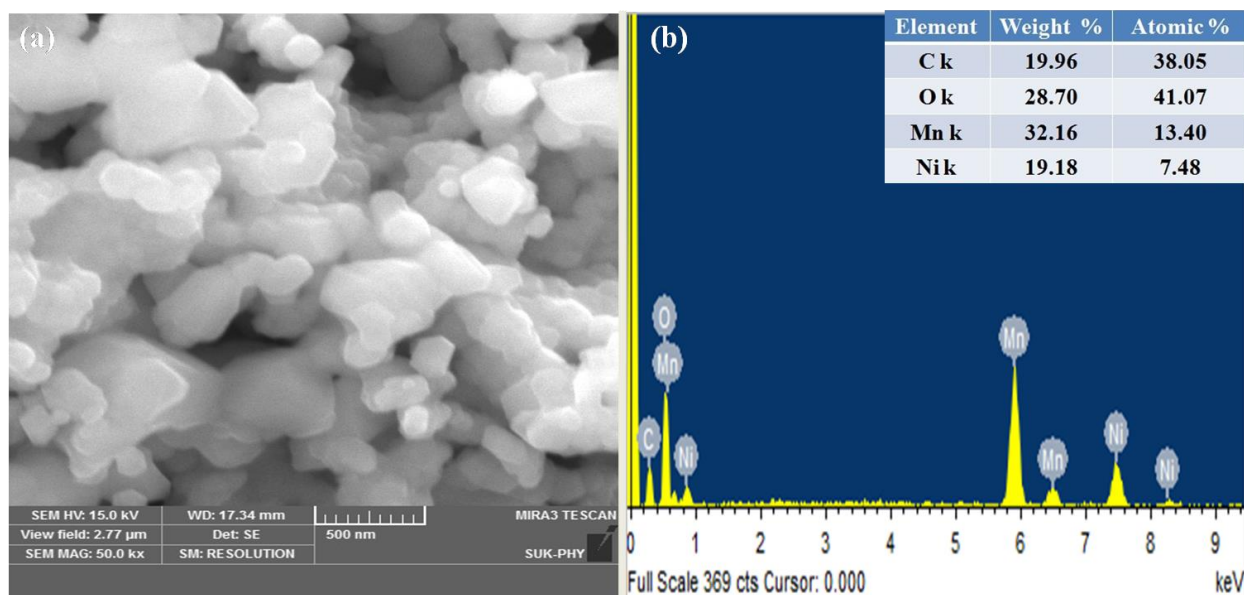| Element	Weight %	Atomic %
C k	19.96	38.05
O k	28.70	41.07
Mn k	32.16	13.40
Ni k	19.18	7.48

Figure 3. (**a**) FESEM and (**b**) elemental analysis of NMO calcined at 800 °C.

In the current research work, Brunauer–Emmett–Teller (BET) measurement was conducted for further investigation of pore size analysis and surface area measurement (shown in Figure 4). The adsorption–desorption plots of NMO clearly indicated type IV isotherm, with a surface area of 18.064 m^2g^{-1}. The observed high surface area of NMO provided a

number of active sites and increased contact between electrolyte and electrode interface [16]. Moreover, Barrett–Joyner–Halenda (BJH) pore size distribution showed (inset of Figure 4) that the average pore size of NMO was 26 nm. It confirmed the mesoporous nature of NMO [21]. Compared to microporous nature, it offered a large number of active sites during the electrochemical reaction. This result leads to an increase in the lithium-ion transfer rate, which is beneficial in improving the electrochemical properties of NMO [16,22].
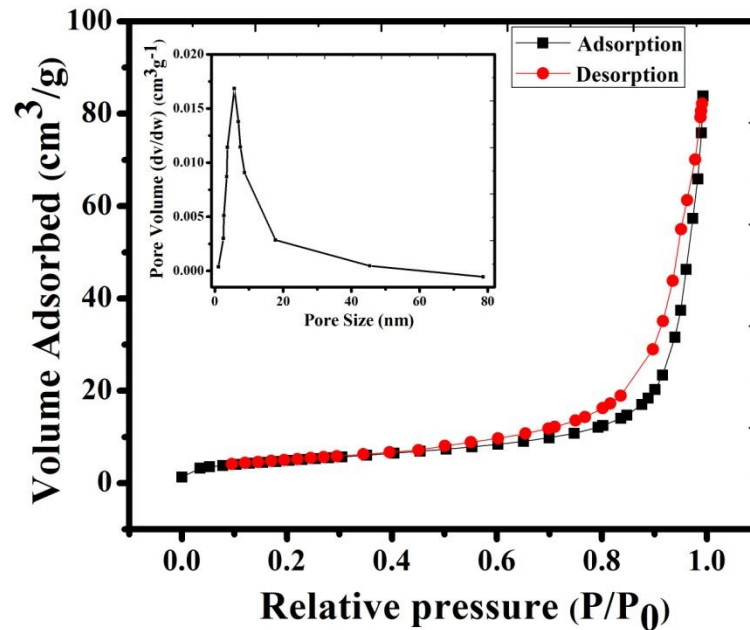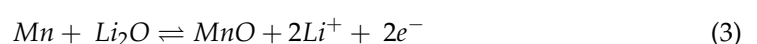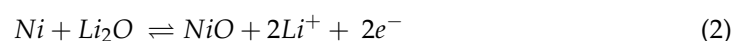

Figure 4. N_2 adsorption–desorption isotherms curve and pore size distribution of NMO calcined at 800 °C.

3.2. Electrochemical Performance

The lithiation delithiation potential and phase transformation of NMO during the electrochemical performance for Li-ion battery was investigated by cyclic voltammetry curve. Figure 5 showed cyclic voltammetry curve at scan rate of 0.1mV/s. In Figure 5, the cathodic peaks centered at ~0.95 was assigned to reduction in Mn^{3+} to Mn^{2+}, and the peak centered at ~0.36 V was assigned to several overlapped electrochemical reaction First one was the reduction in Mn^{2+} or Ni^{2+} to metallic Mn or Ni, respectively [23,24], and second was the irreversible decomposition of the electrolyte to form the solid electrolyte interference (SEI) [25]. During the anodic sweep, the peak centered at ~1.38 was assigned to oxidation of Mn to Mn^{3+}, and the peak centered at ~2.03 V was assigned to oxidation of Ni to Ni^{2+} [24].In addition, redox pair observed at ~0.1 V was assigned to processes related to remaining carbon [26]. The delithiation potential of NMO governed the output voltage and energy density of Li-ion battery, and the higher negative potential of anode ledto lower energy density [27]. In NMO, the reported delithiation potential of NiO was 2.3 V, but in the current research work, it was 2.03 V [27]. These results revealed that the synthesized material has higher energy density. In addition, from Figure 5, it was also seen that the cathodic current is higher compared to the anodic current. This revealed that NMO electrode resist to de-insert lithium ion compared to insertion [14]. Based on the aforementioned cyclic voltammetry analysis, the electrochemical reactions between Li^+ and NMO electrode summarized below [22]

$$NiMn_2O_4 + 8Li + 8e^- = Ni + 2Mn + 4Li_2O \tag{1}$$

$$Ni + Li_2O \rightleftharpoons NiO + 2Li^+ + 2e^- \tag{2}$$

$$Mn + Li_2O \rightleftharpoons MnO + 2Li^+ + 2e^- \tag{3}$$

$$MnO + \frac{1}{3}Li_2O \rightarrow \frac{1}{3}Mn_3O_4 + \frac{2}{3}Li^+ + \frac{2}{3}e^-. \tag{4}$$
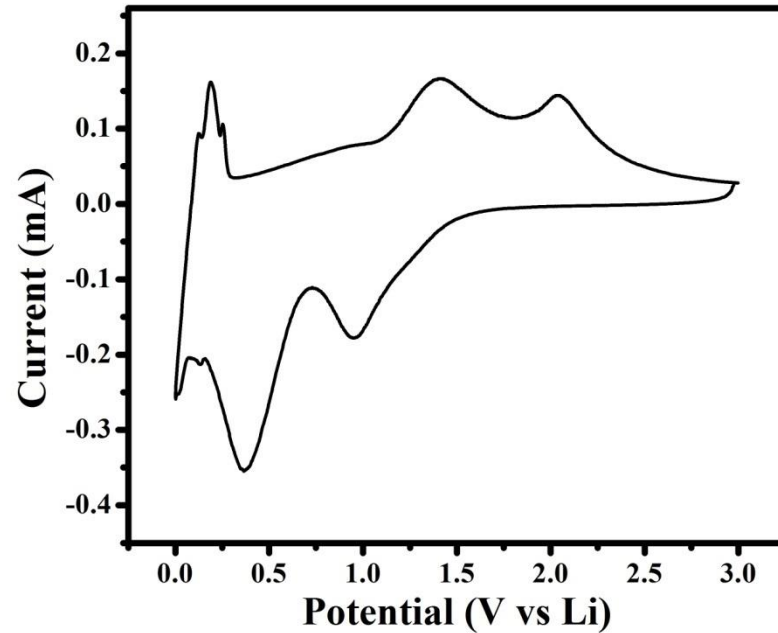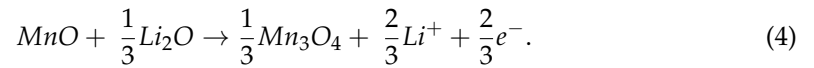

Figure 5. Cyclic voltammetry curve of the NMO electrode at scan rate of 0.1 mV/s.

In addition, cyclic voltammetry curves were recorded at different scan rates. They are shown in Figure 6. The observed cathodic and anodic cell potential showed that with increasing scan rate, cathodic peak potential alters towards lower cell potential and anodic peak potential alters towards higher cell potential. This reveals that in synthesized material, polarization increases with increasing charge–discharge rate [14].
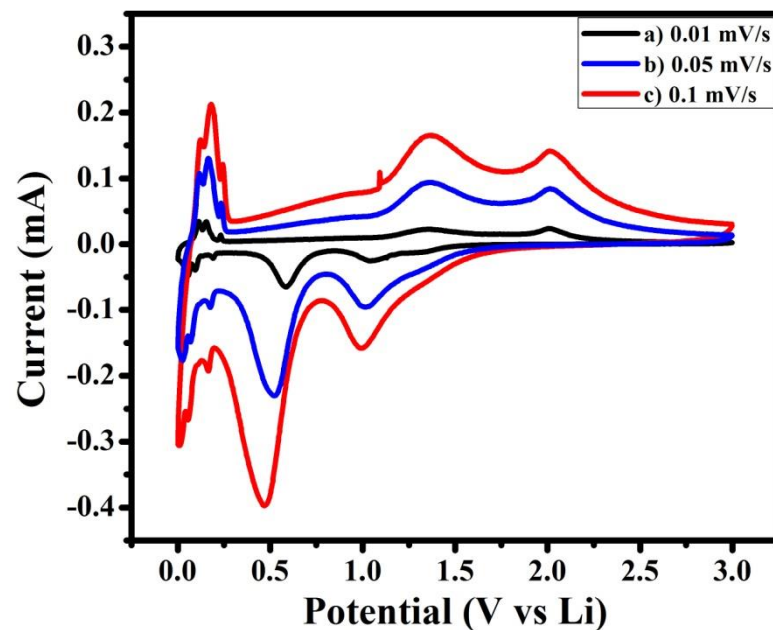

Figure 6. Cyclic voltammetry curves of NMO at different scan rates of (a) 0.01, (b) 0.05, and (c) 0.1 mV/s.

Initial three charge–discharge cycles of NMO at 0.1 A/g in the voltage range of 0.01–3.0 V are showed in Figure 7. The observed discharging capacity of NMO for first,

second, and third cycle was 983, 547, and 555 mA·h/g, respectively. Similar discharge capacity pattern are reported by W. Kang et al. [24] and other results are tabulated in Table 1. After the first cycles, an irreversible capacity loss was observed due to the formation of solid electrolyte interface (SEI) film and reduction in metal oxide with the formation of Li_2O [22]. However, after the first cycle, next cycles were superimposed on each other due to stable structure.
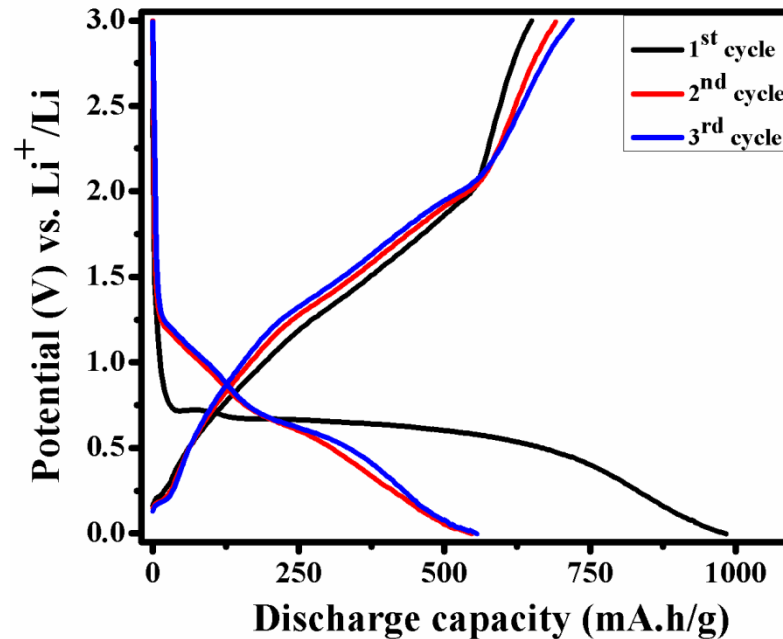

Figure 7. Initial three charge–discharge cycle of NMO at 0.1 A/g.

Table 1. Comparison of specific capacities of $NiMn_2O_4$ and similar material with the literature.

Sr. No.	Material	Synthesizing Method	Specific Capacity (mA·h/g)	Current Density (A/g)	Reference
1.	$NiMn_2O_4$	Citric acid-based combustion method	983	0.1	Present work
2.	$NiMn_2O_4$/rGO	Dipping process	1535	0.1	[22]
3.	$NiMn_2O_4$	Hydrothermal	500	0.1	[22]
4.	$NiMn_2O_4$/C	Solvothermal	1617	0.1	[24]
5.	Fe doped $NiMn_2O_4$	Facile nanocasting method	470	1	[25]
6.	$NiMn_2O_4$	Hydrothermal	1090	0.1	[27]

To study the electrochemical performance of NMO more effectively, its rate performance was investigated (Figure 8). Initially, the NMO electrode was cycled at 0.1 A/g, and the cell delivered average discharge capacity 639 mA·h/g. Then, the current density was increased as 0.2, 0.5, 1, 2, 5, and 10 A/g and the observed average discharged capacitiesare 438, 358, 251, 86, 77, and 35 mA·h/g, respectively. When the NMO electrode was cycled with current density of 1 A/g, after total 35 cycles, it delivered average discharge capacity

of 223 mA·h/g. It showed good reversibility. This result revealed that synthesized material was sustained at a higher current density.
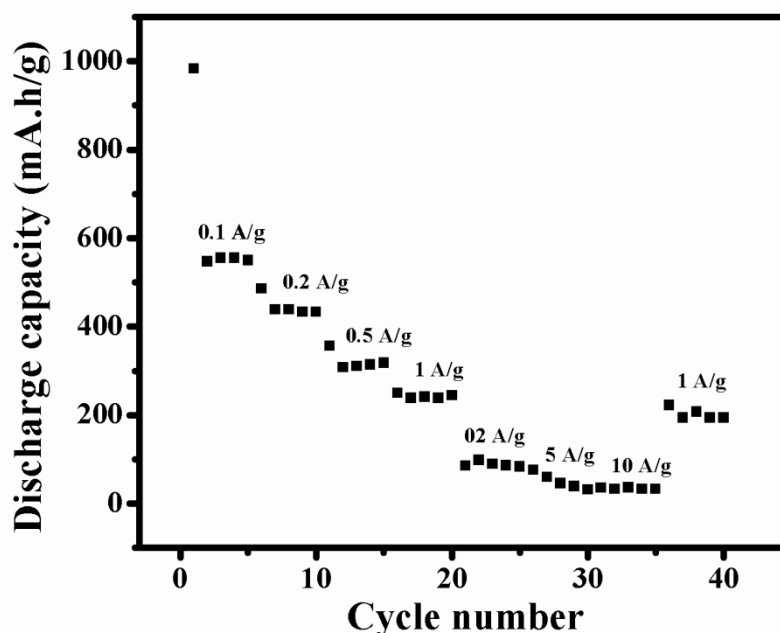

Figure 8. Rate performance of NMO.

Because of crystalline size, surface area, and residual carbon, the synthesized material has good reversibility, rate performance, and stability for its envisaged application in LIBs. The residual carbon present in sp^2 hybridization state can effectively avoid agglomeration in NMO and buffer possible volume change. Furthermore, it reduces lithium-ion diffusion length and provides enough electrons during electron reaction, which help to enhance electrochemical performance.

4. Conclusions

In conclusion, $NiMn_2O_4$ (NMO) nanomaterials are successfully synthesized via citric acid–based combustion method and studied as anode material for lithium-ion battery. BET has revealed the mesoporous nature of NMO with surface area of 18.064 m^2g^{-1}. XPS has revealed after calcination of material at higher temperature that the carbon atom present in citric acid is altered into sp^2 hybridization state. This residual carbon effectively avoids agglomeration, reduces lithium-ion diffusion length, buffers possible volume changes, and provides enough electrons during electron reaction, which lead to enhanced electrochemical performance of NMO. Reduction in Mn^{3+} to Mn^{2+} and Ni^{2+} to Ni is confirmed by the observed cathodic peaks at ~0.99 and 0.46 V in cyclic voltammetry. Besides, anodic sweep oxidation of Mn to MnO and oxidation of Ni to NiO are observed. It exhibits specific discharge capacity of 983 mA·h/g at 0.1 A/g for the first cycle.

References

1. Xu, B.; Qian, D.; Wang, Z.; Meng, Y.S. Recent progress in cathode materials research for advanced lithium ion batteries. *Mater. Sci. Eng. R* **2012**, *73*, 51–65. [CrossRef]
2. Yuan, H.; Wang, X.; Wu, Q.; Shu, H.; Yang, X. Effects of Ni and Mn doping on physicochemical and electrochemical performances of LiFePO$_4$/C. *J. Alloys Compd.* **2016**, *675*, 187–194. [CrossRef]
3. Hu, R.; Zhang, H.; Bu, Y.; Zhang, H.; Zhao, B.; Yang, C. Porous Co$_3$O$_4$ nano fibers surface-modified by reduced graphene oxide as a durable, high-rate anode for lithium ion battery. *Electrochim. Acta* **2017**. [CrossRef]
4. Kulova, T.L.; Kreshchenova, Y.M.; Kuzmina, A.A.; Skundin, A.M.; Stenina, I.A.; Yaroslavtsev, A.B. New high capacity anode materials based on gallium doped lithium titanate. *Mendeleev Commun.* **2016**, *26*, 238–239. [CrossRef]
5. Li, F.; Chen, P.; Wu, H.; Zhang, Y. Cooperative enhancement of electrochemical properties in double carbon decorated Li$_4$Ti$_5$O$_{12}$/C composite as anode for Li-ion batteries. *J. Alloys Compd.* **2015**, *633*, 443–447. [CrossRef]
6. Pathak, R.; Gurung, A.; Elbohy, H.; Chen, K.; Reza, K.; Bahrami, B.; Mabrouk, S.; Ghimire, R.; Hummel, M.; Gu, Z.; et al. Self-Recovery in Li-Metal Hybrid Lithium-Ion Battery via WO$_3$ Reduction. *Nanoscale* **2018**, *10*, 15956–15966. [CrossRef] [PubMed]
7. Goriparti, S.; Miele, E.; Angelis, F.D.; Fabrizio, E.D.; Zaccaria, R.P.; Capiglia, C. Review on recent progress of nano structured anode materials for Li-ion batteries. *J. Power Sources* **2014**, *257*, 421–443. [CrossRef]
8. Cao, K.; Jin, T.; Yang, L.; Jiao, L. Recent progress on conversion reaction metal oxide anodes for Li ion batteries. *Mater. Chem. Front.* **2017**. [CrossRef]
9. Ouyang, Y.; Feng, Y.; Zhang, H.; Liu, L.; Wang, Y. Designing Sandwiched and Crystallized NiMn$_2$O$_4$/C Arrays for Enhanced Sustainable Electrochemical Energy Storage. *ACS Sustain. Chem. Eng.* **2017**, *5*, 196–205. [CrossRef]
10. Bhagwan, J.; Rani, S.; Sivasankaran, V.; Yadav, K.; Sharma, Y. Improved energy storage, magnetic and electrical properties of aligned, mesoporous and high aspect ratio nanofibers of spinel-NiMn$_2$O$_4$. *Appl. Surf. Sci.* **2017**. [CrossRef]
11. Yuvaraj, S.; Selvan, R.K.; Lee, Y.S. An overview of AB2O4- and A2BO4-structured negative electrodes for advanced Li-ion batteries. *RSC Adv.* **2016**. [CrossRef]
12. Chitra, S.; Kalyani, P.; Mohan, T.; Gangadharan, R.; Yebka, B.; Castro-Garcia, S.; Massot, M.; Julien, C.; Eddrief, M. Characterization and Electrochemical Studies of LiMn$_2$O$_4$ Cathode Materials Prepared by Combustion Method. *J. Electroceram.* **1999**, *3*, 433–441. [CrossRef]
13. Rajoba, S.J.; Jadhav, L.D.; Patil, P.S.; Tyagi, D.K.; Varma, S.; Wani, B.N. Enhancement of Electrical Conductivity of LiFePO$_4$ by Controlled Solution Combustion Synthesis. *J. Electron. Mater.* **2017**, *46*, 1683–1691. [CrossRef]
14. Rajoba, S.J.; Jadhav, L.D.; Kalubarme, R.S.; Patil, P.S.; Varma, S.; Wani, B. Electrochemical performance of LiFePO$_4$/GO composite for Li-ion batteries. *Ceram. Int.* **2018**, *44*, 6886–6893. [CrossRef]
15. Phadatare, M.; Patil, R.; Blomquist, N.; Forsberg, S.; Örtegren, J.; Hummelgård, M.; Meshram, J.; Hernández, G.; Brandell, D.; Leifer, K.; et al. Silicon-Nanographite Aerogel-Based Anodes for High Performance Lithium Ion Batteries. *Sci. Rep.* **2019**, *9*, 14621. [CrossRef]
16. Ray, A.; Roy, A.; Ghosh, M.; Ramos-Ramón, J.A.; Saha, S.; Pal, U.; Bhattacharya, S.K.; Das, S. Study on charge storage mechanism in working electrodes fabricated by sol-gel derived spinel NiMn$_2$O$_4$ nanoparticles for supercapacitor application. *Appl. Surf. Sci.* **2019**, *463*, 513–525. [CrossRef]
17. Sahoo, S.; Zhang, S.; Shim, J.-J. Porous Ternary High Performance Supercapacitor Electrode Based on Reduced Graphene Oxide, NiMn$_2$O$_4$, and Polyaniline. *Electrochim. Acta* **2016**, *216*, 386–396. [CrossRef]
18. Rajoba, S.J.; Sartale, S.D.; Jadhav, L.D. Investigating functional groups in GO and r-GO through spectroscopic tools and effect on optical properties. *Opt. Int. J. Light Electron Opt.* **2018**, *175*, 312–318. [CrossRef]
19. Zhang, M.; Guoa, S.; Zheng, L.; Zhang, G.; Haoc, Z.; Kang, L.; Liu, Z. Preparation of NiMn$_2$O$_4$ with large specific surface area from an epoxide driven sol gel process and its capacitance. *Electrochim. Acta* **2013**, *87*, 546–553. [CrossRef]
20. Wang, Z.; Zhu, Z.; Zhang, C.; Xu, C.; Chen, C. Facile synthesis of reduced graphene oxide/NiMn$_2$O$_4$ nano rods hybrid materials for high performance super capacitors. *Electrochim. Acta.* **2017**, *230*, 438–444. [CrossRef]
21. Kim, M.R.; Kalla, R.M.N.; Kim, S.; Kim, M.R.; Kim, I. NiMn$_2$O$_4$ nano-sheet decorated hierarchically porous polyaromatic carbon spheres for high performance super capacitors. *ChemElectroChem* **2017**. [CrossRef]
22. Huang, J.; Wang, W.; Lin, X.; Gu, C.; Liu, J. Three dimensional sandwich structured NiMn$_2$O$_4$/reduced graphene oxide nano composites for highly reversible Li-ion battery anodes. *J. Power Sources* **2018**, *378*, 677–684. [CrossRef]
23. Li, L.; Yao, Q.; Liu, J.; Ye, K.; Liu, B.; Liu, Z.; Yang, H.; Chen, Z.; Duan, J.; Zhang, B. Porous Hollow Super lattice NiMn$_2$O$_4$/NiCo$_2$O$_4$ Meso crystals as a Highly Reversible Anode Material for Lithium Ion Batteries. *Front. Chem.* **2018**, *6*, 153. [CrossRef] [PubMed]
24. Kang, W.; Tang, Y.; Li, W.; Yang, X.; Xue, H.; Yang, Q.; Lee, C. High interfacial storage capability of porousNiMn2O4/C hierarchical tremella-like nanostructures as lithium ion battery anode. *Nanoscale* **2015**, *7*, 225–231. [CrossRef]
25. Ma, Y.; Tai, C.-W.; Younesi, R.; Gustafsson, T.; Lee, J.Y.; Edström, K. Iron Doping in Spinel NiMn$_2$O$_4$: Stabilization of the Meso porous Cubic Phase and Kinetics Activation toward Highly Reversible Li$^+$ Storage. *Chem. Mater.* **2015**. [CrossRef]
26. Thauer, E.; Ottmann, A.; Schneider, P.; Möller, L.; Deeg, L.; Zeus, R.; Wilhelmi, F.; Schlestein, L.; Neef, C.; Ghunaim, R.; et al. Filled Carbon Nanotubes as Anode Materials for Lithium-Ion Batteries. *Molecules* **2020**, *25*, 1064. [CrossRef] [PubMed]
27. Zhao, S.; Li, H.; Jian, Z.; Xing, Y.; Zhang, S. Selfassembled hierarchical porous NiMn$_2$O$_4$ microspheres as high performance Li-ion battery anodes. *RSC Adv.* **2018**, *8*, 41749–41755. [CrossRef]